

THE SANTA FE LIGHT CONE SIMULATION PROJECT: I. CONFUSION AND THE WHIM IN UPCOMING SUNYAEV-ZEL'DOVICH EFFECT SURVEYS

ERIC J. HALLMAN^{1,2}, BRIAN W. O'SHEA³, JACK O. BURNS², MICHAEL L. NORMAN⁴, ROBERT HARKNESS⁵ & RICK WAGNER⁴

Draft version October 24, 2018

ABSTRACT

We present the first results from a new generation of simulated large sky coverage (~ 100 square degrees) Sunyaev-Zeldovich effect (SZE) cluster surveys using the cosmological adaptive mesh refinement N-body/hydro code Enzo. We have simulated a very large ($512^3 h^{-3} \text{Mpc}^3$) volume with unprecedented dynamic range. We have generated simulated light cones to match the resolution and sensitivity of current and future SZE instruments. Unlike many previous studies of this type, our simulation includes unbound gas, where an appreciable fraction of the baryons in the universe reside.

We have found that cluster line-of-sight overlap may be a significant issue in upcoming single-dish SZE surveys. Smaller beam surveys ($\sim 1'$) have more than one massive cluster within a beam diameter 5-10% of the time, and a larger beam experiment like Planck has multiple clusters per beam 60% of the time. We explore the contribution of unresolved halos and unbound gas to the SZE signature at the maximum decrement. We find that there is a contribution from gas outside clusters of $\sim 16\%$ per object on average for upcoming surveys. This adds both bias and scatter to the deduced value of the integrated SZE, adding difficulty in accurately calibrating a cluster Y-M relationship.

Finally, we find that in images where objects with $M > 5 \times 10^{13} M_{\odot}$ have had their SZE signatures removed, roughly a third of the total SZE flux still remains. This gas exists at least partially in the Warm Hot Intergalactic Medium (WHIM), and will possibly be detectable with the upcoming generation of SZE surveys.

Subject headings: cosmology: theory–galaxies:clusters:general–cosmology:observations–hydrodynamics–methods:numerical–cosmology:cosmic microwave background

1. INTRODUCTION

Clusters of galaxies form from the highest peaks in the primordial spectrum of density perturbations generated by inflation in the early universe. They are the most massive virialized structures in the universe, and as such are rare objects. The number density of galaxy clusters as a function of mass and redshift is strongly dependent on a number of cosmological parameters. In particular, counting the abundance of clusters above some lower mass limit as a function of cluster redshift places constraints on Ω_b , Ω_M , σ_8 , and the dark energy equation of state parameter, w (Wang & Steinhardt 1998; Haiman et al. 2001).

Observational measurement of the cluster abundance over large sky areas and redshift range is required to generate cosmological parameter constraints which are complementary to constraints from the cosmic microwave background (CMB), type Ia supernovae, Big Bang nucleosynthesis (BBN), the Lyman- α forest, and galaxy redshift surveys (Tozzi 2006). Cluster survey yields depend

on the value of the minimum cluster luminosity probed as a function of redshift, the scaling between cluster luminosity and mass, the growth function of structure, and the redshift evolution of the comoving volume element, all of which depend on a complex combination of cosmological parameters (Rosati et al. 2002) and intracluster medium (ICM) physics (Evrard 2004).

1.1. Sunyaev-Zel'dovich Effect Surveys

The Sunyaev-Zel'dovich Effect (Sunyaev & Zeldovich 1972) is a process by which the hot electrons trapped in the large dark matter potential wells of clusters inverse Compton scatter CMB photons to higher energy, resulting in a low frequency (< 218 GHz) decrement, and a corresponding high frequency (> 218 GHz) increment in the CMB on the angular scale of the cluster. The strength of the SZE decrement/increment is characterized by the Compton y parameter, which results from the line of sight integral of the thermal pressure

$$y = \int \sigma_T n_e \frac{k_b T}{m_e c^2} dl, \quad (1)$$

where n_e is the electron density and T is the gas electron temperature. We also define the integrated Compton y parameter as

$$Y = \int y dA \quad (2)$$

which is the integration over the area subtended by a circle corresponding to some relevant cluster physical radius. The observed temperature fluctuation correspond-

arXiv:0704.2607v3 [astro-ph] 29 Aug 2007

¹ National Science Foundation Astronomy and Astrophysics Postdoctoral Fellow

² Center for Astrophysics and Space Astronomy, Department of Astrophysics and Planetary Sciences, University of Colorado at Boulder, Boulder, CO 80309; hallman, burns@casa.colorado.edu

³ Theoretical Astrophysics (T-6), Los Alamos National Laboratory, Los Alamos, NM 87545; bwoshea@lanl.gov

⁴ Center for Astrophysics and Space Sciences, University of California at San Diego, La Jolla, CA 92093; mnorman, rpwagner@cosmos.ucsd.edu

⁵ San Diego Supercomputing Center, MC0505, 9500 Gilman Drive, La Jolla, CA 92093; harkness@sdsu.edu

ing to a give value of y in a given frequency band is

$$\frac{\Delta T}{T} = yg(x), \quad (3)$$

where

$$g(x) = \left(x \frac{e^x + 1}{e^x - 1} - 4 \right) [1 + \delta_{sze}(x, T_e)], \quad (4)$$

$x = h\nu/kT_{cmb}$ and δ_{SZE} is a relativistic correction as described in Itoh & Nozawa (2004). For our purposes in this paper we have neglected the relativistic correction, but will explore it in future work. This correction is small (less than 1% at the maximum decrement frequency) for clusters with $T < 10$ keV.

The SZE is particularly useful in cosmological studies due to its near redshift independence (Rephaeli 1995; Birkinshaw 1999; Carlstrom et al. 2002). Therefore, observations of clusters are not limited to low redshift as in the X-ray, but can extend to as high as $z \sim 2$, where the number of massive clusters becomes small. An additional consequence of the redshift independence of SZE surveys is that a flux-limited survey is also approximately a mass limited survey (Rephaeli 1995; Haiman et al. 2001). These two properties make SZE surveys uniquely valuable for cluster abundance counts and determination of the cluster mass function with redshift, provided one can obtain independent optical redshifts for the galaxies in the identified objects. The near redshift independence of the SZE creates unique complications for large area surveys which do not seriously affect other types of surveys (e.g., optical and X-ray). In particular, the contribution to the sky signal from both low mass and distant halos, as well as unbound gas, may be a significant source of confusion.

There are several upcoming millimeter wavelength cluster surveys with new telescopes including the Atacama Pathfinder Experiment Sunyaev-Zeldovich survey (APEX-SZ) (Güsten et al. 2006), the South Pole Telescope (SPT) (Ruhl et al. 2004), and the Atacama Cosmology Telescope (ACT) (Fowler 2004), in addition to the space-based *Planck* Surveyor (Murdin 2000), which will conduct large blind surveys of clusters using the SZE. Table 1 shows the values of the relevant instrumental characteristics for the single-dish survey telescopes we have taken from the literature and used in the following analysis. For this study, we limit ourselves to results using a single band, ~ 144 GHz, where the SZE decrement is maximal, though these results will generalize to other bands and to multiwavelength studies, since the SZE from all gas will have roughly the same spectral signature (modified slightly by relativistic effects). However, for removing contaminating signals (e.g. radio point sources, CMB) multiwavelength coverage will be very desirable.

The variation in survey characteristics for these instruments has important consequences for cluster surveys. For example, the distribution of sources detected as a function of cluster redshift should be different for each survey. This is because although the SZE surface brightness does not diminish with distance, the angular size of the objects does vary with redshift, and may be larger or smaller than the instrument beam for any given cluster. This selection effect is modified also by the volume sam-

TABLE 1
CHARACTERISTICS OF UPCOMING SZE SURVEYS

Survey	Angular Coverage	Beam Size (~ 144 GHz)	RMS per beam
APEX-SZ	TBD	1.0'	10 μ K
SPT	4000 deg ²	1.0'	10 μ K
ACT	100 deg ²	1.7'	2 μ K
Planck	All-Sky	7.1'	6.0 μ K

pled as a function of redshift in a fixed angular field and the growth rate of structure in an Λ CDM universe. It is important to understand these selection effects in order to constrain cosmology. We must be able to determine the correct distribution of clusters as a function of redshift from the surveys or systematic errors in estimated cosmological parameters will result.

There are also several centimeter wave (≈ 30 GHz) interferometers that are performing surveys of the SZE, such as the Arcminute Microkelvin Imager (AMI) (Holler 2000) and the Sunyaev-Zel'dovich Array (SZA) (Loh et al. 2005). SZE surveys have the potential to strongly constrain the w parameter for dark energy, since they sample clusters to large redshift.

Determining the abundance and distribution in mass and redshift of massive galaxy clusters from observables is a challenging exercise. In the realm of cluster abundance counts, one needs to know with high precision the mass range of clusters probed in a flux-limited survey as a function of cluster redshift. This determination depends on detailed knowledge of the scaling between mass and light in clusters. It is critical to understand how cluster observables correlate with cluster total mass in order to use clusters of galaxies as precision cosmological tools.

1.2. The Role of Simulations in Understanding Cluster Surveys

Recent results indicate that high resolution N-body simulations (Warren et al. 2006; Heitmann et al. 2006; Reed et al. 2005) generate mass functions which differ significantly from the Press-Schechter result and also from the subsequent modifications of Sheth & Tormen (1999) and Jenkins et al. (2001). Since there is strong evidence that purely analytic methods are insufficient, “precision cosmology” requires the use of numerical simulations. In other words, in order to make predictions which match the observed cluster population to percent-level precision, analytic methods are inadequate.

The output of numerical simulations of clusters can be compared to the observed cluster mass function. This comparison is non-trivial, however, due to the uncertain nature of the conversion between observable quantities (e.g., X-ray luminosity, SZE Compton y parameter, lensing shear) and cluster total mass. Observations of the cluster gas typically depend on the detailed properties of the hot baryons in clusters. It has been shown by our group and others that cluster observables have a strong dependence on the baryonic physics in the ICM (Hallman et al. 2006; Nagai 2006), and are subject to an array of uncertainties. However, the SZE signal integrated over the projected cluster area (as defined in Equation 2) inside r_{500} is unique in that the general scaling with mass is relatively independent of the assumed

gas physics (Motl et al. 2005; Nagai 2006). While the normalization of the Y-M relation has some dependence on ICM physics, the slope and tightness of the correlation are unaffected (Nagai 2006). Most recent simulated light cone calculations use the dark matter mass function generated by large N-body simulations like the Hubble Volume simulation or the Millennium run, with “painted on” baryons to generate mock surveys (e.g., Evrard et al. 2002; Geisbüsch et al. 2005). These studies typically assume the gas is isothermal and in hydrostatic equilibrium with the dark matter potential.

Both simulations including relevant physics (e.g., White 2003; Rasia et al. 2006; Hallman et al. 2006) and high resolution X-ray observations of galaxy clusters (e.g., Vikhlinin et al. 2005; Markevitch et al. 2002; Hallman & Markevitch 2004) suggest that many clusters depart strongly from both equilibrium and isothermality. These deviations can have a strong impact on both the observable and derived properties of clusters. Thus, in order to properly simulate sky surveys, it is critically important to self-consistently include baryons in numerical simulations. While some work has been done in this area (e.g., Springel et al. 2001; White et al. 2002; Roncarelli et al. 2006, 2007), the largest volumes simulated were small ($\sim 100\text{-}200\text{ h}^{-1}\text{Mpc}$), and only sufficient to generate synthetic light cones of roughly $1\text{-}4\text{ deg}^2$. The simulation performed for this study models a significantly larger physical volume than previous efforts, has a higher peak physical resolution, and fully incorporates baryons self-consistently. This allows us to perform much larger synthetic surveys ($\sim 100\text{ deg}^2$) than could be done with earlier N-body/hydro simulations.

Cosmological N-body/hydro simulations have advanced significantly in the last decade, such that the simulation output now compares quite well to observations of galaxy clusters (Springel et al. 2006). In particular, our group and others have shown that there is good agreement in simulated and observed scaling relations between bulk cluster ICM properties (e.g., cluster mass, X-ray luminosity, X-ray spectral temperature) (Motl et al. 2004). There remain important differences, particularly for lower mass clusters, which indicates the need for a better understanding of the details of baryonic cluster physics. The advance of realism in simulations is a result of diligent, iterative efforts by various groups of investigators to directly compare simulations to observations. This study uses a large volume high resolution adiabatic simulation, and serves as a template for more complex runs involving additional non-gravitational physical processes which are likely important to accurately modeling cluster surveys. These results should be relatively robust in any case, as it has been shown that SZE survey yields are relatively independent of cluster physics details (White et al. 2002).

1.3. Modeling SZE Surveys

A variety of approaches have been taken to model SZE surveys. Most involve either semi-analytic prescriptions or N-body simulations where the gas is added in a post processing step (e.g., Schulz & White 2003). As discussed in the previous section, there are limitations to these methods, particularly in the assumptions of hydrostatic equilibrium and isothermality. Some studies (e.g., White et al. 2002; Holder et al. 2007) have discussed the

contribution of unresolved clusters/groups to the signature of detected clusters. The presence of gas outside the cluster virial radii in low density unbound structures such as filaments is potentially also quite important. This gas is completely absent in non-hydrodynamic treatments of the simulation volume, appears naturally in our calculation, and is expected to contain 40-50% of the baryons in the universe (Cen & Ostriker 2006). Since the SZE does not diminish with distance, and results from a line of sight integral of the gas pressure, the sum of all the flux from unbound gas could be a significant contributor to the total flux in any cluster detection.

In this paper, we have examined the contribution of line-of-sight baryonic gas to the expected SZE signal of simulated clusters. We have stacked a $(512\text{ h}^{-1}\text{Mpc})^3$ volume (comoving) adaptive mesh refinement (AMR) N-body/hydro simulation to generate a survey of a light cone subtending 100 square degrees on the sky. Our simulated survey covers a larger sky area, and at higher angular resolution, than any previous N-body + hydro simulated survey.

There is extensive work in the literature on cluster detection algorithms for SZE surveys, (e.g., Diego et al. 2002; Herranz et al. 2002; Hobson & McLachlan 2003; Schäfer et al. 2006; Melin et al. 2006). These methods involve various techniques designed to spatially filter out the primary CMB anisotropies (so called matched filtering), wavelet techniques, and application of public tools such as SExtractor⁶ (Bertin & Arnouts 1996). We find the existing work to be quite detailed, and do not introduce new algorithms of this type here. Indeed, it is important to step back from the analyses which have attempted to include all the relevant contaminants and instrumental effects and explore the intrinsic difficulties resulting from the cluster population as projected on the sky. There is a limiting precision one can expect from cluster surveys irrespective of the ability to remove instrumental effects, point source confusion and sky backgrounds. This limit results from the possibly irreducible confusion due to clusters, groups, lower mass halos and unbound gas, all of which contribute to the SZE signal with a nearly identical spectral signature. This study examines these effects with a more realistic cosmological calculation than has typically been done, including the full complement of baryons expected in the real universe.

We explore the intrinsic limitations of SZE surveys by comparing and characterizing the contribution of unresolved halos and unbound filamentary gas to the cluster signal in samples that might result from upcoming surveys using a full hydro/N-body simulation of the cluster sky. In future work, we will model backgrounds and instrumental characteristics as has been done in the literature recently (e.g., Sehgal et al. 2006; Melin et al. 2006; Schäfer et al. 2006) with a focus on techniques for accurately extracting cluster properties and abundance.

We discuss our methodology of simulating these large surveys in Section 2, analytic predictions of SZE observables in Section 3, present results in Section 4, discussion in Section 5, and summarize our work in Section 6.

2. METHODOLOGY

2.1. The Enzo Code

⁶ http://terapix.iap.fr/rubrique.php?id_rubrique=91/

‘Enzo’⁷ is a publicly available, extensively tested adaptive mesh refinement cosmology code developed by Greg Bryan and colleagues (Bryan & Norman 1997a,b; Norman & Bryan 1999; O’Shea et al. 2004, 2005). The specifics of the Enzo code are described in detail in these papers (and references therein), but we present a brief description here for clarity.

The Enzo code couples an N-body particle-mesh (PM) solver (Efsthathiou et al. 1985; Hockney & Eastwood 1988) used to follow the evolution of a collisionless dark matter component with an Eulerian AMR method for ideal gas dynamics by Berger & Colella (1989), which allows high dynamic range in gravitational physics and hydrodynamics in an expanding universe. This AMR method (referred to as *structured* AMR) utilizes an adaptive hierarchy of grid patches at varying levels of resolution. Each rectangular grid patch (referred to as a “grid”) covers some region of space in its *parent grid* which requires higher resolution, and can itself become the parent grid to an even more highly resolved *child grid*. Enzo’s implementation of structured AMR places no fundamental restrictions on the number of grids at a given level of refinement, or on the number of levels of refinement. However, owing to limited computational resources it is practical to institute a maximum level of refinement, ℓ_{max} . Additionally, the Enzo AMR implementation allows arbitrary integer ratios of parent and child grid resolution, though in general for cosmological simulations (including the work described in this paper) a refinement ratio of 2 is used.

Since the addition of more highly refined grids is adaptive, the conditions for refinement must be specified. In Enzo, the criteria for refinement can be set by the user to be a combination of any or all of the following: baryon or dark matter overdensity threshold, minimum resolution of the local Jeans length, local density gradients, local pressure gradients, local energy gradients, shocks, and cooling time. A cell reaching any or all of the user-specified criteria will then be flagged for refinement. Once all cells of a given level have been flagged, rectangular solid boundaries are determined which minimally encompass them. A refined grid patch is then introduced within each such bounding volume, and the results are interpolated to a higher level of resolution.

In Enzo, resolution of the equations being solved is adaptive in time as well as in space. The timestep in Enzo is satisfied on a level-by-level basis by finding the largest timestep such that the Courant condition (and an analogous condition for the dark matter particles) is satisfied by every cell on that level. All cells on a given level are advanced using the same timestep. Once a level L has been advanced in time Δt_L , all grids at level $L+1$ are advanced, using the same criteria for timestep calculations described above, until they reach the same physical time as the grids at level L . At this point grids at level $L+1$ exchange baryon flux information with their parent grids, providing a more accurate solution on level L . Cells at level $L+1$ are then examined to see if they should be refined or de-refined, and the entire grid hierarchy is rebuilt at that level (including all more highly refined levels). The timestepping and hierarchy rebuilding process is repeated recursively on every level to the

maximum existing grid level in the simulation.

Two different hydrodynamic methods are implemented in Enzo: the piecewise parabolic method (PPM) (Woodward & Colella 1984), which was extended to cosmology by Bryan et al. (1995), and the hydrodynamic method used in the ZEUS magnetohydrodynamics code (Stone & Norman 1992a,b). We direct the interested reader to the papers describing both of these methods for more information, and note that PPM is the preferred choice of hydro method since it is higher-order-accurate and is based on a technique that does not require artificial viscosity, which smoothes shocks and can smear out features in the hydrodynamic flow.

2.2. Simulation Setup and Analysis

The simulation discussed in this paper is set up as follows. We initialize our calculation at $z = 99$ assuming a cosmological model with $\Omega_m = 0.3$, $\Omega_b = 0.04$, $\Omega_{CDM} = 0.26$, $\Omega_\Lambda = 0.7$, $h = 0.7$ (in units of 100 km/s/Mpc), $\sigma_8 = 0.9$, and using an Eisenstein & Hu (1999) power spectrum with a spectral index of $n = 1$. The simulation is of a volume of the universe $512 \text{ h}^{-1} \text{ Mpc}$ (comoving) on a side with a 512^3 root grid. The dark matter particle mass is $7.228 \times 10^{10} \text{ h}^{-1} \text{ M}_\odot$ and the mean baryon mass resolution is $1.112 \times 10^{10} \text{ h}^{-1} \text{ M}_\odot$. The simulation was then evolved to $z = 0$ with a maximum of 7 levels of adaptive mesh refinement (a maximum spatial resolution of 7.8 h^{-1} comoving kpc), refining on dark matter and baryon overdensities of 8.0 (to ensure an approximately Lagrangian mass resolution in baryonic structures). The equations of hydrodynamics were solved with the Piecewise Parabolic Method (PPM) using the dual energy formalism. The entire grid hierarchy (including both particle and baryon information) was written out at regular intervals, and in particular, data was output at intervals of $\Delta z = 0.25$ between $z = 3$ and $z = 2.5$ (inclusive), and $\Delta z = 0.1$ between $z = 2.5$ and $z = 0.1$ (inclusive).

Analysis was performed on every data output between $z = 3$ and $z = 0.1$ in an identical way. The HOP halo-finding algorithm (Eisenstein & Hut 1998) was applied to the dark matter particle distribution to produce a dark matter halo catalog. Spherically-averaged, mass-weighted radial profiles of various baryonic and dark matter quantities including density, temperature, and pressure were then generated for every halo in the catalog with an estimated halo mass greater than $4 \times 10^{13} \text{ M}_\odot$. These radial profiles were used to calculate more accurate virial masses and radii as well as an estimate for the Compton y parameter as a function of impact parameter on the halo. Projections of the integrated Compton y value along the line of sight were created for each of the three axes along the simulation volume, with two projections per axis – one of the front half of the simulation volume, and one along the back half. Each projection has an approximate depth of $\Delta z = 0.1$. These projections have a resolution of 2048 pixels on a side.

2.3. Generation of the “Santa Fe” Light Cone

Mock SZE observations of a $10^\circ \times 10^\circ$ patch of sky are generated by stacking projections from the simulation discussed in Section 2.2. These “light cones” are created by stacking projections of the Compton y parameter at each redshift output. At each redshift, the

⁷ <http://lca.ucsd.edu/portal/software/enzo/>

projection is chosen to be along a random axis, and has been randomly shifted in space such that the positions of large scale structure is uncorrelated. Additionally, the projections have been rescaled to the resolution of the light cone, which is 2048 pixels per side, or a resolution of 17.58 arc seconds per pixel. This scaling may involve tiling (for redshifts where $512 \text{ h}^{-1} \text{ Mpc}$ comoving corresponds to less than 10° on the sky) or interpolating (for redshifts where $512 \text{ h}^{-1} \text{ Mpc}$ comoving corresponds to more than 10° on the sky). Secondary maps are created which include only the Compton y parameter contributed by gas within the virial radius of halos with masses above $5 \times 10^{13} M_\odot$, and only gas outside of the virial radius of these objects. 200 of these mock “light cones” at this size and resolution are created using different random seeds. These light cones (named “Santa Fe” light cones due to the location where the project was conceived) have angular resolution which is significantly higher than any current or proposed SZE observational campaign. *The goal of this analysis is not to determine an optimal method for source finding, but to determine the contamination from unresolved halos and unbound gas for a simple method.*

3. ANALYTIC PREDICTIONS FOR SZE OBSERVABLES

Here we describe some of the theory behind the use of SZE cluster observations in constraining cosmology. Though we are aware that these types of analytic calculations have been performed previously, we show them here to motivate not just the current analysis, but that which will be performed for subsequent papers in this series.

One of the most useful methods for retrieving cosmological information from SZE observations of galaxy clusters is by the calculation of galaxy cluster counts as a function of redshift. The number of galaxy clusters above some given minimum mass $M_{min}(z)$ in a redshift bin of width dz and solid angle $d\Omega$ can be defined using the Press-Schechter formalism (Press & Schechter 1974) as

$$\frac{dN}{dzd\Omega}(z) = \frac{dV}{dzd\Omega}(z) \int_{M_{min}(z)}^{\infty} dM \frac{dn}{dM}(M, z) \quad (5)$$

where $dV/dz d\Omega$ is the cosmological comoving volume element at a given redshift, and $\frac{dn}{dM} dM$ is the comoving halo number density as a function of mass and redshift. The latter is expressed as by Jenkins et al. (2001) as

$$\frac{dn}{dm}(M, z) = -0.315 \frac{\rho_0}{M} \frac{1}{\sigma_M} \frac{d\sigma_M}{dm} \exp[-|0.61 - \log(D(z)\sigma_M)|^{3.8}] \quad (6)$$

where σ_M is the RMS density fluctuation, computed on mass scale M from the $z = 0$ linear power spectrum (Eisenstein & Hu 1999), ρ_0 is the mean matter density of the universe, defined as $\rho_0 \equiv \Omega_m \rho_c$ (with ρ_c being the cosmological critical density, defined as $\rho_c \equiv 3H_0^2/8\pi G$), and $D(z)$ is the linear growth function, given by this fitting function:

$$D(z) = \frac{1}{1+z} \frac{5\Omega_m(z)}{2} \left\{ \Omega_m(z)^{4/7} - \Omega_\Lambda(z) + \left[1 + \frac{\Omega_m(z)}{2} \right] \left[1 + \frac{\Omega_\Lambda(z)}{70} \right] \right\}^{-1} \quad (7)$$

(Carroll et al. 1992), with $\Omega_m(z)$ and $\Omega_\Lambda(z)$ defined as:

$$\Omega_m(z) = \Omega_{m,0}(1+z)^3 E^{-2}(z) \quad (8)$$

and

$$\Omega_\Lambda(z) = \Omega_{\Lambda,0} E^{-2}(z) \quad (9)$$

where $\Omega_{m,0}$ and $\Omega_{\Lambda,0}$ are the density of matter and cosmological constant at the present day, expressed in units of the critical density. The cosmological volume element is given by:

$$\frac{dV}{dzd\Omega}(z) = \frac{c}{H_0} \frac{(1+z)^2 D_A^2}{E(z)} \quad (10)$$

where $D_A(z)$ is the angular diameter distance as a function of redshift, c is the speed of light, H_0 is the Hubble parameter at $z = 0$, and $E(z)$ is given by:

$$E^2(z) = \Omega_{m,0}(1+z)^3 + \Omega_\Lambda \quad (11)$$

in a flat universe with a cosmological constant (Peebles 1993). The RMS amplitude of the density fluctuations as function of mass at any redshift, as smoothed by a spherically symmetric window function with a characteristic comoving radius R , can be computed from the matter power spectrum using the relation:

$$\sigma^2(M, z) = \int_0^\infty \frac{dk}{k} \frac{k^3}{2\pi^2} P(k, z) |\tilde{W}_R(k)|^2 \quad (12)$$

where $\tilde{W}_R(k)$ is the Fourier transform of the real-space top hat smoothing function:

$$\tilde{W}_R(k) = \frac{3}{k^3 R^3} [\sin(kR) - kR \cos(kR)] \quad (13)$$

The radius R is calculated for a given mass by using the relation $M = \frac{4}{3}\pi R^3 \Omega_m \rho_c$, and $\sigma(M, z)$ is normalized to σ_8 , defined as the RMS density fluctuation when smoothed by a sphere with a comoving radius of $8 \text{ h}^{-1} \text{ Mpc}$ at $z = 0$, using observations of large-scale structure or the cosmic microwave background. The matter power spectrum is expressed as:

$$\frac{k^3}{2\pi^2} P(k, z) = \left(\frac{ck}{H_0} \right)^{3+n} T^2(k) \frac{D^2(z)}{D^2(0)} \quad (14)$$

where $T(k)$ is the matter transfer function which describes the way in which the processing of the initial spectrum of matter density fluctuations during the radiation-dominated era (Peebles 1993) and $D(z)$ is the fitting function for the linear growth function, as given in Equation 7. In the calculations discussed in this paper, we use the transfer function $T(k)$ provided by Eisenstein & Hu (1999).

Figure 1 shows the number of galaxy clusters per square degree as a function of redshift with $M_{tot} \geq 1 \times 10^{14} \text{ h}^{-1} M_\odot$ in the WMAP Year III “most favored” cosmology ($\Omega_m = 0.268$, $\sigma_8 = 0.776$) and in the cosmology used in the simulation in this paper ($\Omega_m = 0.3$, $\sigma_8 = 0.9$). Due to the higher Ω_m and σ_8 , significantly more galaxy clusters are expected to be seen in this simulation than one would expect given the WMAP Year III result.

Figure 2 shows the number of galaxy clusters per square degree as a function of redshift with $M_{tot} \geq 1 \times 10^{14} \text{ h}^{-1} M_\odot$ for a variety of cosmological models.

Panel (a) shows a sequence of cosmologies where all parameters except σ_8 are held constant, using the same cosmological parameters as in the simulation described in this paper ($\Omega_m = 0.3$, $\Omega_b = 0.04$, $\Omega_\Lambda = 0.7$, $h = 0.7$, $n = 1$), but varying σ_8 from 0.6 to 1.2 in steps of 0.1 (bottom to top lines). Panel (b) shows a sequence of cosmologies where all parameters except Ω_m and Ω_Λ are held constant using the same cosmological parameters as in the simulation described in this paper ($\Omega_b = 0.04$, $h = 0.7$, $n = 1$, $\sigma_8 = 0.9$), but varying Ω_m from 0.2 to 0.4 in steps of 0.05 (bottom to top lines), and keeping $\Omega_\Lambda = 1 - \Omega_m$. It is interesting to note that varying σ_8 while holding all other cosmological parameters results in a change in both the overall number of halos (a factor of more than 3 between WMAP and the cosmology in our simulation) and the redshift at which the distribution peaks. Both effects can be explained by examining the term in the exponent in equation 6. The comoving number density of halos is maximized when $0.61 - \log(D(z)\sigma_M) = 0$, or $D(z) \times \sigma_M \simeq 4.07$. For a given set of cosmological parameters, increasing σ_8 increases σ_M for a given mass value, and thus maximizes the number density of halos at a given mass at a smaller linear growth factor (or, more intuitively, a higher redshift). Variation in Ω_m and Ω_Λ while holding all other parameters constant effectively results in a change in the normalization of the overall halo number density, while keeping the redshift at which this distribution peaks roughly constant.

These results are of great interest for upcoming SZE surveys, which will sample clusters to relatively low mass at high redshifts ($z = 0.5-1.0$) compared to optical and X-ray surveys. This redshift range is where we should expect the largest difference between a low σ_8 cosmology preferred by WMAP and a higher value typically used in cosmological simulations. The large difference between the abundance of clusters in these different cosmologies should lead to large differences in the number of identified clusters in surveys. This means that very early on in any SZE survey it should become fairly obvious which cosmology is preferred by cluster observations. This will be an even stronger constraint when optical follow up observations are used to determine redshifts, which will break the degeneracy between Ω_M and σ_8 .

4. RESULTS

4.1. Simulated Mass Function

One of the most basic tests of the correctness of a cosmological simulation is whether or not it can match the predicted halo mass function for a given cosmology. This is particularly important in the context of creating simulated sky maps for cosmological surveys of any kind, given that the number of halos and their redshift distribution is the most basic test of cosmological properties. Figure 3 shows the cumulative number density of cosmological halos as a function of mass for several redshifts which span the range of interest for the topics discussed in this work ($z = 0.1 - 3$). The halos were found as described in Section 2.2, and the masses used are the total halo virial mass (including both baryons and dark matter), rather than the mass returned by the Hop halo finding algorithm (Eisenstein & Hut 1998). We also show the fitting function for cumulative halo number density obtained by Warren et al. (2006) as a reference. At low

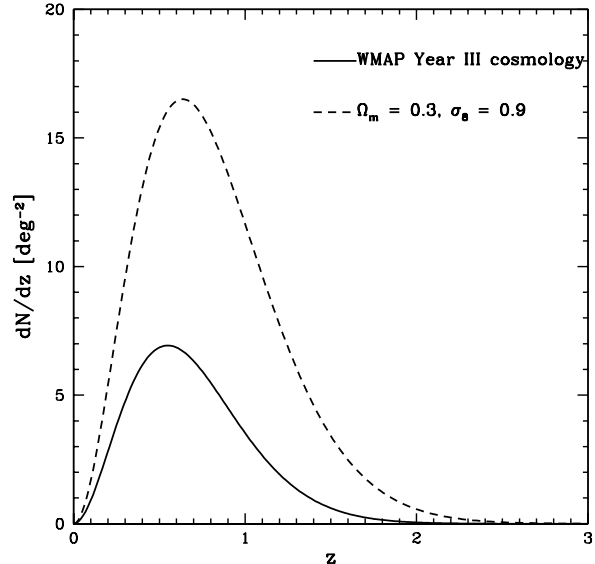


FIG. 1.— Number of galaxy clusters per square degree as a function of redshift with $M_{tot} \geq 1 \times 10^{14} h^{-1} M_\odot$ in the WMAP Year III “most favored” cosmology (solid line; $\Omega_m = 0.268$, $\sigma_8 = 0.776$) and the cosmology used in the simulation in this paper (dashed line; $\Omega_m = 0.3$, $\sigma_8 = 0.9$). The distribution peaks at $z \simeq 0.55$ for the WMAP Year III cosmology and at $z \simeq 0.64$ for the cosmology used in the simulations in this paper.

redshifts ($z = 0.1 - 1$) the mass function of halos from the simulation agrees quite well with the fitting function over the mass range of interest. This is encouraging, as the bulk of galaxy clusters in the universe are at these low redshifts (as shown in Figure 1). At higher redshifts ($z = 2$), the fitting function and halo mass function only agree at the highest masses ($M_{halo} \geq 10^{14} h^{-1} M_\odot$). This is to be expected: grid-based codes, including adaptive mesh codes, tend to suppress low-mass halo formation, particularly at high redshift, as has been seen in recent code comparisons (O’Shea et al. 2005; Heitmann et al. 2005). This suppression in our study only exists due to the choice of simulation setup. In order to model such a large physical volume with both N-body + hydrodynamics, we must sacrifice mass resolution due to computational effort concerns. Given that the cosmological surveys of interest will only be sensitive to halos in the mass range where this simulation agrees well with the Warren et al. fit, and the relative paucity of these halos at $z \gtrsim 2$, there is little cause for concern.

4.2. SZE Angular Power Spectrum

We have calculated angular power spectra for the 200 survey images to determine the cosmic variance in this field, and the general form of the power spectrum. The calculation involves determining the power spectral density of the image as a function of image scale. Additionally, we have performed the same calculation on maps smoothed with the beam size at 144 GHz for each of four upcoming SZE survey instruments. We have modified the images to model the limitations of these instruments in a simple way. First, for each instrument, we have gaussian smoothed the image with the FWHM of the beam at a wavelength (frequency) of 2.1mm (144

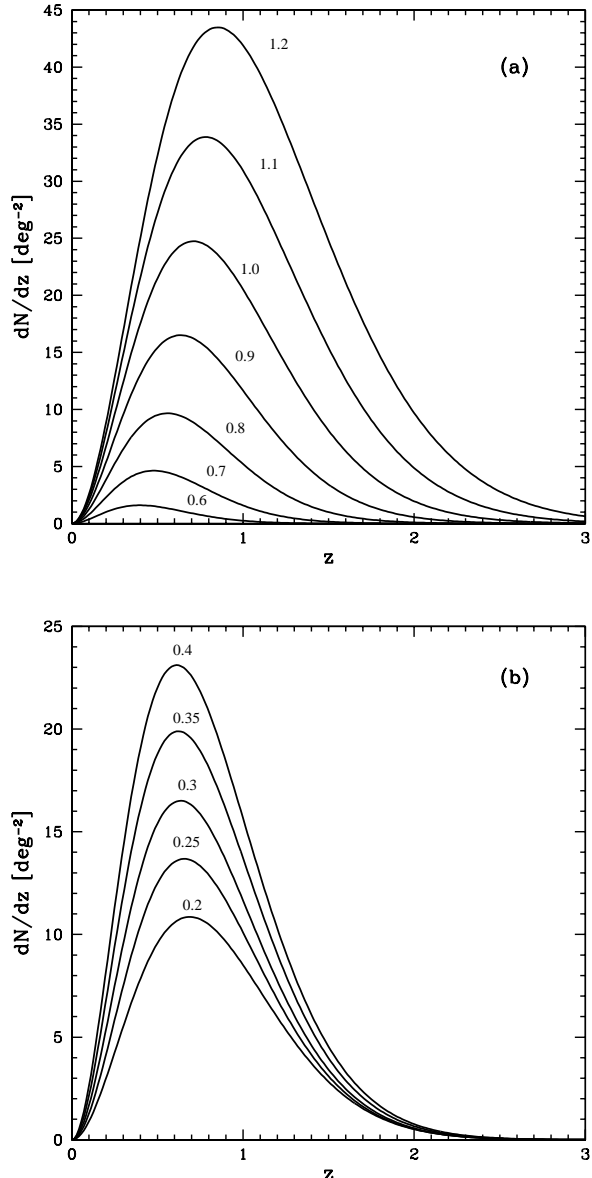


FIG. 2.— Number of galaxy clusters per square degree as a function of redshift with $M_{tot} \geq 1 \times 10^{14} h^{-1} M_{\odot}$ for a variety of cosmologies. Panel (a): All parameters except σ_8 are held constant, using the same cosmological parameters as in the simulation described in this paper ($\Omega_m = 0.3$, $\Omega_b = 0.04$, $\Omega_{\Lambda} = 0.7$, $h = 0.7$, $n = 1$), but varying σ_8 from 0.6 to 1.2 in steps of 0.1 (bottom to top lines). Panel (b): All parameters except Ω_m and Ω_{Λ} are held constant using the same cosmological parameters as in the simulation described in this paper ($\Omega_b = 0.04$, $h = 0.7$, $n = 1$, $\sigma_8 = 0.9$), but varying Ω_m from 0.2 to 0.4 in steps of 0.05 (bottom to top lines) and keeping $\Omega_{\Lambda} = 1 - \Omega_m$.

GHz) corresponding to the maximum SZE decrement. All the upcoming SZE single-dish surveys will have the capability of operating at this wavelength. We have also rebinned each image such that the beam diameter is represented by at least two pixels in order to be Nyquist sampled. A “background” in each case is generated by adding a gaussian distributed variation with a FWHM equal to each survey’s stated limiting sensitivity.

The result of our analysis of the power spectrum of

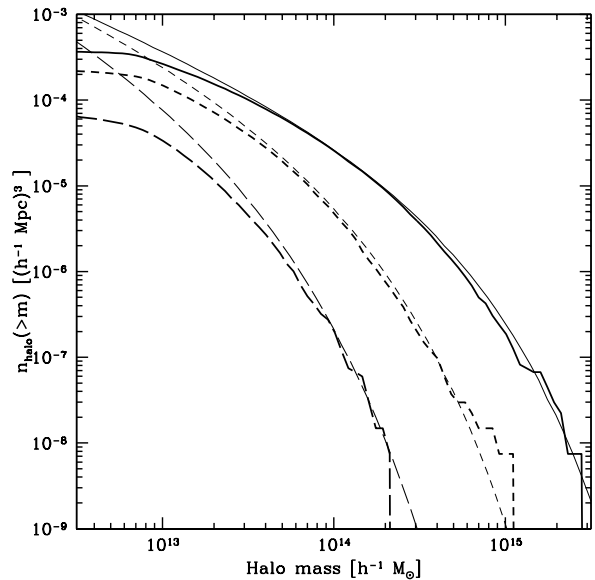


FIG. 3.— Cumulative number density at several redshifts. Solid: $z = 0.1$. Short-dashed: $z = 1.0$. Long-dashed: $z = 2$. Thick lines are simulation results calculated using the halo virial masses (dm+gas) and the thin lines are the Warren fitting function (Warren et al. 2006).

the simulated SZE surveys is shown in Figure 4. The solid lines are the mean values of the power from the 200 stacking realizations of the light cone, and the dotted lines indicate the range in which 90% of our simulated light cone power spectra fall. The color indicates which survey’s characteristics were used to generate the result.

The location of the peak of each curve is a function of the resolving power of the survey, as is its amplitude, in that the power at the smallest angular scale for each survey is different. The cyan line (labeled SWH01) is the result obtained by Springel et al. (2001) with a 1 degree angular scale light cone generated from an SPH N-body/hydro simulation run with cosmological parameters matching our simulation. The raw power spectrum is generated with no smoothing from the raw light cone survey images. The SWH01 result is different from ours, possibly a result of lower spatial resolution in the simulation (resulting in a deficit in the small scale angular power) and had a smaller angular field (1 square degree) than ours, leading to a higher ℓ cutoff ($\ell=400$) than we show ($\ell=70$). As has been shown previously, and specifically in Figure 4 of Springel et al. (2001), analytic predictions of the SZE power vary widely depending on the calculation method. They neither agree with the simulation results, nor in many cases with each other. It seems that the analytic result has not converged, and so to avoid confusion we do not plot it in this work.

It is clear that each survey will sample a slightly different range of scales, though they obviously all are able to measure the large angular scale power. Each power spectrum peaks and turns over where the angular scale of the beam begins to limit the measurement at high ℓ . The power spectrum is not very sensitive to non-gravitational gas physics at low multipole numbers, but primarily is sensitive to cosmology, particularly the value of σ_8 (White et al. 2002; Holder et al. 2007). The addi-

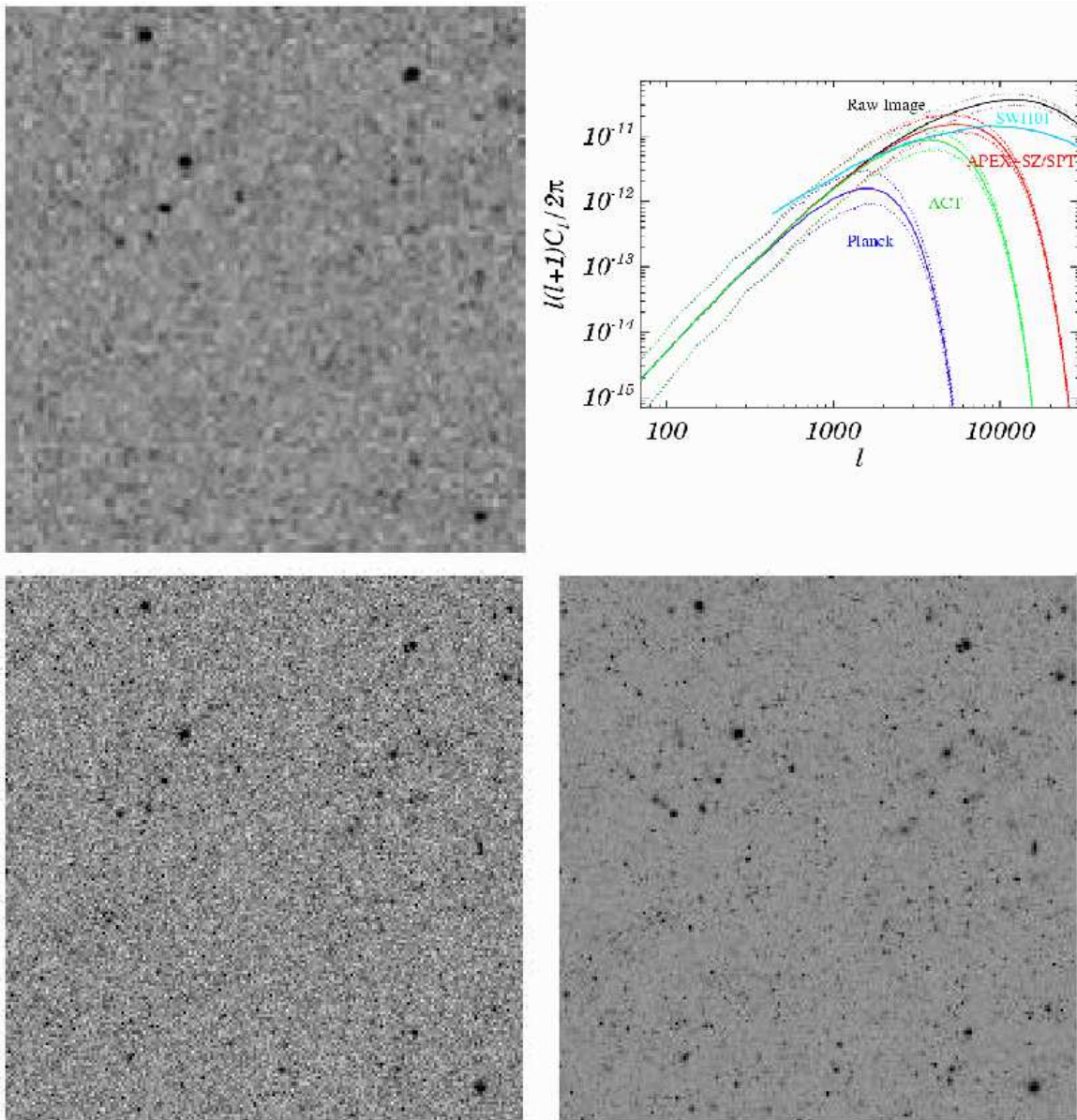


FIG. 4.— Upper Left: Light cone survey image of 100 square degrees modified to simulate the beam size and limiting sensitivity of the Planck Surveyor all-sky survey at 144 GHz ($7.1'$, $6\mu\text{K}$). Upper right: Angular power spectra generated from these images. Lower left: Light cone image modified to simulate APEX-SZ/SPT survey characteristics at ~ 144 GHz ($1.0'$, $10\mu\text{K}$). Lower right: Light cone image modified to simulate ACT survey ($1.7'$, $2\mu\text{K}$). Numbers in parentheses indicate (beam size, survey sensitivity/beam) at 144 GHz.

tion of non-gravitational physics does impact the small scale power however, for example Holder et al. (2007) show that preheating results in reduced small scale power in their simulated images.

What is also of interest in this analysis is the size of the variance shown by the 90% range error bars. On 100 square degree patches of the sky at $\ell \lesssim 2000$ the deduced power can be different by factors of 5-8. This indicates that the power spectrum can be quite different from one area of the sky to another, and clearly requires greater sky coverage to be well constrained. The cosmic variance range does not become very small until $\ell \gtrsim$ a few thousand.

4.3. SZE Source Identification

To identify objects in the light cone images, we simply locate the projected clusters from the three-dimensional

halo finding in the image plane. Since we design the shifting and stacking strategy, it is trivial to determine the image plane location of each cluster in each redshift slice of the light cone. We also have calculated the spherically averaged radial profiles projected into the image plane of the Compton y -parameter. For each cluster with $M \geq 10^{14}M_{\odot}$, we can then calculate the integrated value of Y (when comparisons to analytic results are not performed, we use true masses on the simulation grid, without the h^{-1} modifier). The result is shown in Figure 5. In this case, we have integrated out to the virial radius of each cluster. We show the variance in 200 stacking realizations of the simulated light cone, indicating the increase in variation at high flux, as expected due to rare, very massive objects projected into some fraction of the images.

We are also interested in the redshift distribution of the

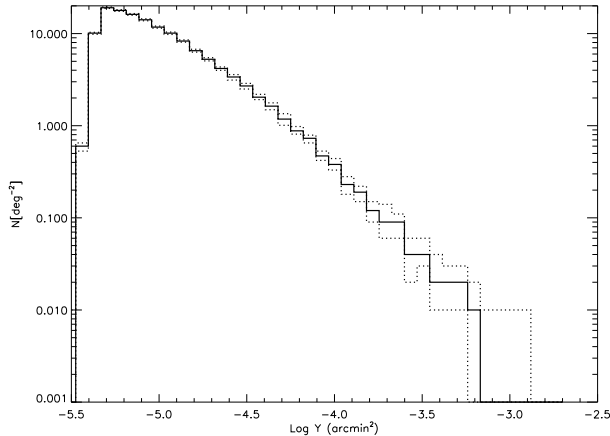


FIG. 5.— Plot of number of objects per square degree in the simulated survey image as a function of integrated Compton y parameter. Dotted lines are 90% variance as calculated from 200 stacking realizations of the light cone.

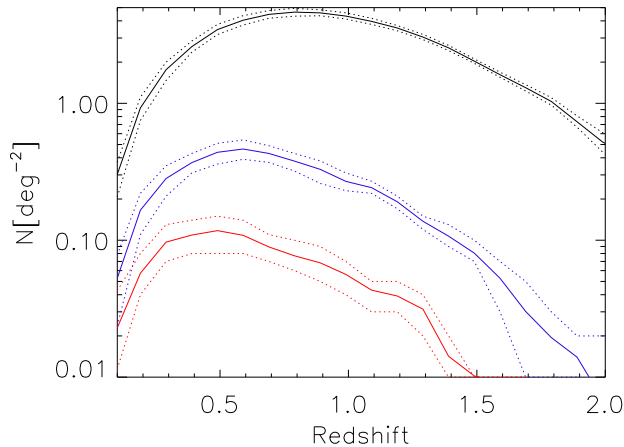


FIG. 6.— Angular density of clusters in the light cone images as a function of redshift. Black solid line is the redshift distribution of clusters with $M \geq 10^{14} M_{\odot}$. Blue solid line is for $M \geq 3.0 \times 10^{14} M_{\odot}$, red is for $M \geq 5.0 \times 10^{14} M_{\odot}$. Dotted lines are 90% variance of 200 independent stacking realizations of the light cone.

objects, which can be compared to analytic estimates. The result of this analysis is shown in Figure 6. In each case, we have taken the mean value and plotted it as a solid line, and the 90% variance in 200 light cone realizations as dotted lines. The black lines indicate all clusters with total masses above $10^{14} M_{\odot}$ in the simulation which are in the projected field of the survey. Blue and red lines are for clusters above higher mass cutoffs, blue for $M \geq 3.0 \times 10^{14} M_{\odot}$ and red for $M \geq 5.0 \times 10^{14} M_{\odot}$. These give a rough indication of the expected redshift distribution of identified clusters in upcoming surveys.

For one projected light cone image, we show the Y vs M relationship in Figure 7. In this case, Y is calculated by integrating the value of Compton y in the image out to each cluster’s *projected* virial radius. The value of Y is corrected for redshift since it depends on $E(z)^{-2/3}$ (see Nagai 2006) due to the cosmological dependence of the cluster M - T relation, and the angular scale is converted to Mpc through use of the value of

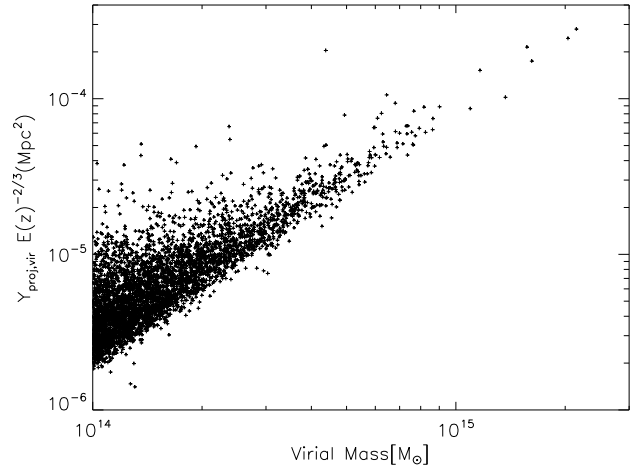


FIG. 7.— Projected integrated Y value plotted against cluster mass. Y is integrated from the simulated light cone survey images from the center of each cluster out to the projected virial radius. Y is converted from angular units using the angular diameter distance appropriate to the redshift of the matched simulated cluster. Y is also scaled with $E(z)^{-2/3}$ to account for the cosmological variation of the mass scaling relation.

D_A for each cluster. Contrast this plot with Figure 8, for a single realization of the light cone image, where the true projected Y is plotted against cluster true mass from the simulation. The true value for Y is calculated from the projected spherically averaged radial profiles of each simulated cluster, but includes the gas out only to the virial radius *in three dimensions*. This true relation has extraordinarily tight scatter, as has been shown previously (da Silva et al. 2000; Motl et al. 2005; Nagai 2006). The difference in the two plots is effectively the difference between the cluster’s true integrated SZE and the SZE integrated in a cylinder with radius equal to the cluster’s virial radius. For a narrow mass bin around $3.0 \times 10^{14} M_{\odot}$, the median bias in Y due to projection is 79%, and the scatter is +32%/-16% about that median, a significant increase over the scatter in the true Y - M relationship. Note that some clusters in Figure 7 appear to have lower value of Y in projection than the true value for that cluster. These are the clusters which lie near the edge of the simulated survey image, and the cluster extends beyond the image edge. As identified by other studies, errors in extracting the correct value of Y should dominate the error budget for this relation (e.g., White et al. 2002; Melin et al. 2006). These figures illustrate the difficulty in accurately estimating Y from observations. A similar result is noted by White et al. (2002) using data from a smoothed particle hydrodynamics (SPH) simulation. We have corrected the primary object in the source region for cosmological evolution in the M - T relation, so the remaining scatter results from line of sight projection effects. This means that there are secondary bound objects (and unbound gas) which are projected into the cluster’s source region as will be described in the next section.

4.4. Confusion Problems

In this section we address the confusion resulting from clusters, groups, and smaller mass halos, as opposed to confusion resulting from radio and millimeter wave point

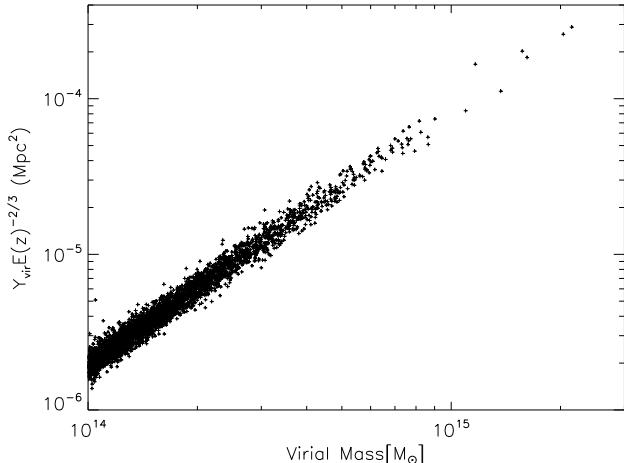


FIG. 8.— Integrated Compton y vs Total mass relationship extracted directly from the simulation data. Y is the projected integrated SZE y parameter from each cluster out the the virial radius, total mass is from the simulation grid for each object. Y is also scaled with $E(z)^{-2/3}$ to account for the cosmological variation of the mass scaling relation.

sources in the cluster fields. This work also includes the additional flux contributed by unbound gas, which contributes at some level in the real universe, but has been ignored in most simulations of SZE surveys. While there are several definitions of confusion in the literature, even for SZE surveys, we have chosen to define cluster confusion as the number of true cluster- or group-mass objects in the simulation whose centers are within the source region in projection. Since upcoming SZE surveys are unlikely to detect cluster gas out to the virial radius, we have chosen a smaller radius (r_{500}) as the source region. For each of the upcoming surveys, we have defined the source region as a radius of a full beam diameter, presuming that if two objects were imaged by two separate non-overlapping beams, that there is a possibility they would not be confused. This also presumes that the secondary object is bright enough to be detected on its own. One can also define confusion as an error in recovered flux (Holder et al. 2007) from sources found by progressive matched filtering at different angular scales corresponding to variation of the angular size of clusters as a function of redshift (e.g., Melin et al. 2006).

Whether this type of confusion can be mitigated depends on a variety of factors, including the mass of the additional secondary objects in the source region, redshift distribution and angular scale of the objects and the observing beam and multiple wavelength identification of the objects (e.g., optical, X-ray, lensing). We endeavor here then simply to characterize the amount of said confusion, leaving the mitigation of this problem to future work. Figure 9 shows for each of the surveys considered a histogram of the number of objects above $10^{14}M_{\odot}$ in the source regions (as defined above) of all clusters with $M \geq 3.0 \times 10^{14}M_{\odot}$. These mass limits are chosen somewhat arbitrarily, though for the ground-based surveys, $3.0 \times 10^{14}M_{\odot}$ is close to the expected mass limit. $10^{14}M_{\odot}$ is chosen for the contaminating objects on the expectation that one or more object above that mass in the source region should lead to a significant bias

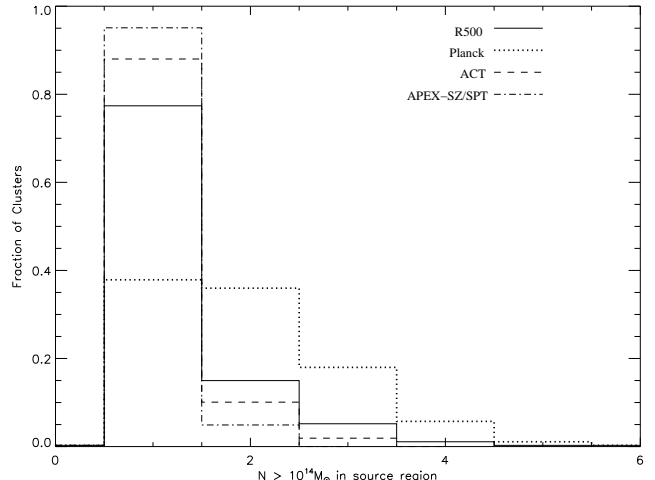


FIG. 9.— Histogram of number of simulated clusters with $M > 10^{14}M_{\odot}$ per source region for each of survey modified light cones. Source region is defined as inside r_{500} projected for the solid line, and as within 1 beam diameter (at 144 GHz) distance for each of the survey instruments listed. Cluster identifications for all 200 light cones are tallied and used in the fraction.

in the SZE flux from that expected from a single cluster in the detectable mass range. As in Section 4.3, we have identified each cluster by its projected image plane position associated with its true three-dimensional location in the simulation after stacking. It is clear that for Planck, there are a high number of objects per source region above this relatively high mass. In fact, roughly 40% of source regions have only one object above this mass cut, while nearly 60% have more than one. Contrast this result with that of APEX/SPT, where 95% of source regions have only one massive cluster projected into them. This result is clearly correlated directly with beam size, but also depends weakly on sensitivity, since a deeper survey will lead to larger source regions (when limited by signal-to-noise) and will increase the chance of objects overlapping into the source, and can also increase “bridging” between sources. Also, it is likely that SZE experiments will sometimes detect a source where there is no cluster in the mass range at that location (spurious detections). Therefore our estimates shown in Figure 9 may be optimistic.

4.5. Contribution of Unresolved Halos and Unbound Gas

One possibly significant difference between this and other similar simulation-based studies is the inclusion of adiabatic hydrodynamics in addition to N-body dynamics in the calculation. This results in several advantages over N-body calculations that include the effects of baryons in the post-processing phase. The first is that our clusters need not be in hydrostatic equilibrium (HSE) which is a standard assumption in dark matter-only simulations which have been post-processed. Both simulations and observations indicate that hydrostatic equilibrium is not a safe assumption for many clusters (see e.g., Rasia et al. 2005; Markevitch et al. 2002). A significant amount of scatter in cluster observables results from the disequilibrium caused by mergers (Roettiger et al. 1996; Ricker & Sarazin 2001; Randall et al. 2002). This scatter is absent in N-body + HSE type studies, and is nat-

urally included in our work. Secondly, our simulations include baryons which are outside virialized objects, including gas in filaments and voids. The SZE in particular is sensitive to this additional gas, since the effect is only linear in the gas density and is relatively redshift independent. Thus any gas along the line of sight contributes to the SZE integral, and is not diminished by distance.

While several authors have noted that the angular power in the SZE from the cluster subtracted field is small (see, e.g., Holder et al. 2007), it is not necessarily true that the total SZE flux (or decrement) from unresolved halos and unbound gas is negligible. Figure 10 shows an image of the full field of light cone in projected Compton y parameter next to an image of the field where clusters with $M > 5.0 \times 10^{13} M_{\odot}$ have been removed from the field. We show in Figure 11 the angular power from the SZE in the cluster subtracted images compared to the power due to the full SZE image. At small scales ($\ell > 5000$), the power in the cluster subtracted image is more than an order of magnitude lower than that of the full image. At larger scales, however, the difference narrows, and in fact the 90% variance overlaps for the two in some regions. This is likely due partly to incomplete cluster subtraction in the image.

A significant result from this analysis is that roughly one third of the SZE flux in the image comes from objects with $M < 5.0 \times 10^{13} M_{\odot}$ and filamentary structures made up of gas in the Warm-Hot Intergalactic Medium (WHIM) phase. Figure 12 shows a histogram for 200 independent light cone realizations from our simulations of the ratio of the total SZE flux (or integrated Compton y parameter) in the 100 deg² field from only gas within the virial radius of those clusters to that of all other gas in the field. Thus, we predict that upcoming SZE instruments are the only near-term telescopes that will possibly be capable of detecting WHIM over large sky areas. This result is consistent with Hernández-Monteagudo et al. (2006), who have performed a similar study with a fixed grid N-body/hydro simulation with considerably lower peak resolution (195 h⁻¹ kpc) than our work.

It is important to note that in an adiabatic simulation, gas fractions are relatively constant with cluster/group mass. In the real universe, as well as in more realistic simulations such as those we performed for Hallman et al. (2006), the ICM gas radiatively cools and forms stars, lowering the gas fraction of the cluster, and effectively attenuating its SZE signal. This effect is also cluster-mass dependent, lower mass objects have comparatively lower gas fractions. Within a simulation with radiative cooling and star formation prescriptions, we find gas fractions 30-50% lower in clusters with $M \approx 10^{14} M_{\odot}$ than the average value for clusters with $M > 3 \times 10^{14} M_{\odot}$. Additionally, recent observational studies (e.g., McCarthy et al. 2007) point out that gas fractions deduced from X-ray data decrease with cluster temperature (therefore with mass), by of order 50% for 1-2 keV clusters from a flat value above ~ 4 keV. Therefore we expect our result here to be an upper limit on the amount of flux from low mass objects and WHIM gas, possibly above the true value by as much as a factor of two. Our future light cone simulations will be run with non-gravitational physics, and we will explore the effect on the SZE background.

4.6. Contribution per Source of Cluster Subtracted Images

Since unresolved halos ($M < 5 \times 10^{13} M_{\odot}$) and unbound gas in this simulation clearly contribute flux to the image, it is important to ask how much additional flux per source is added. This extra flux is a bias, in that it is always additive. Therefore it should boost the emission of all clusters in the field by some amount which may vary from cluster to cluster, adding both bias and scatter to the cluster SZE observable. This effect is critical to understand, since photometric accuracy of the SZE in clusters is key to calibrating a Y-M relationship which will be useful in determining cosmological parameters. The precision of the calibration of the Y-M relationship depends strongly on its scatter (Melin et al. 2006).

Figure 13 shows the ratio of the integrated Compton y parameter inside a cylinder of radius r_{500} around each cluster above $10^{14} M_{\odot}$ from the cluster subtracted image to the value for the full image. The plot shows values for clusters in a single light cone image, but there is very little variation in the mean, median and scatter across all the realizations. The large scatter is partly a result of incomplete subtraction of the cluster SZE signature from the image, but also results from variations in large scale structure in the various source regions. What is clear from the plots is that there is a systematic bias in integrated Compton y resulting from low mass objects and unbound gas. The mean value of this ratio is $16.3^{+7.0}_{-6.4}\%$. The 1σ scatter is $\pm 30-40\%$. It is unclear that this bias is reducible, since identifying objects of very low mass in source fields, particularly at high redshift, seems prohibitively difficult. Additionally, making direct observation of filamentary gas, particularly to locate its position on the sky, has been nearly impossible.

There will be some variation from survey to survey in this additional flux. Depending on how much of the cluster's radial extent is sampled, the mean value for all clusters will change. The scatter though, is quite large, which means that accounting for this flux is not as simple as removing a uniform background from each cluster's SZE signal. In our study we also performed the identical analysis for the clusters, assuming detection out to r_{2500} , and found no change in the scatter, though the mean value of the additional flux dropped to roughly 8-10%. As discussed in previous sections, a more realistic modeling of the heating and cooling in the ICM should result in a reduction in this additional flux (or decrement) by as much as 30-50%. Even with a reduction of this size, we still expect it to be a few percent to 10% effect with of order $\pm 30-40\%$ scatter, creating challenges for a percent-level calibration of the Y-M relationship.

5. DISCUSSION AND SUMMARY

In this study, we have taken an important step missing from previous work in the literature on characterizing selection functions of SZE surveys. In earlier work, investigators have attempted to evaluate methods of removing contamination of the galaxy cluster SZE signal due to the CMB and other point sources and backgrounds. However, they have included only the baryons present in clusters and groups, and artificially inserted the gas in hydrostatic equilibrium with the dark matter distribution from an N-body only simulation. Here, we have

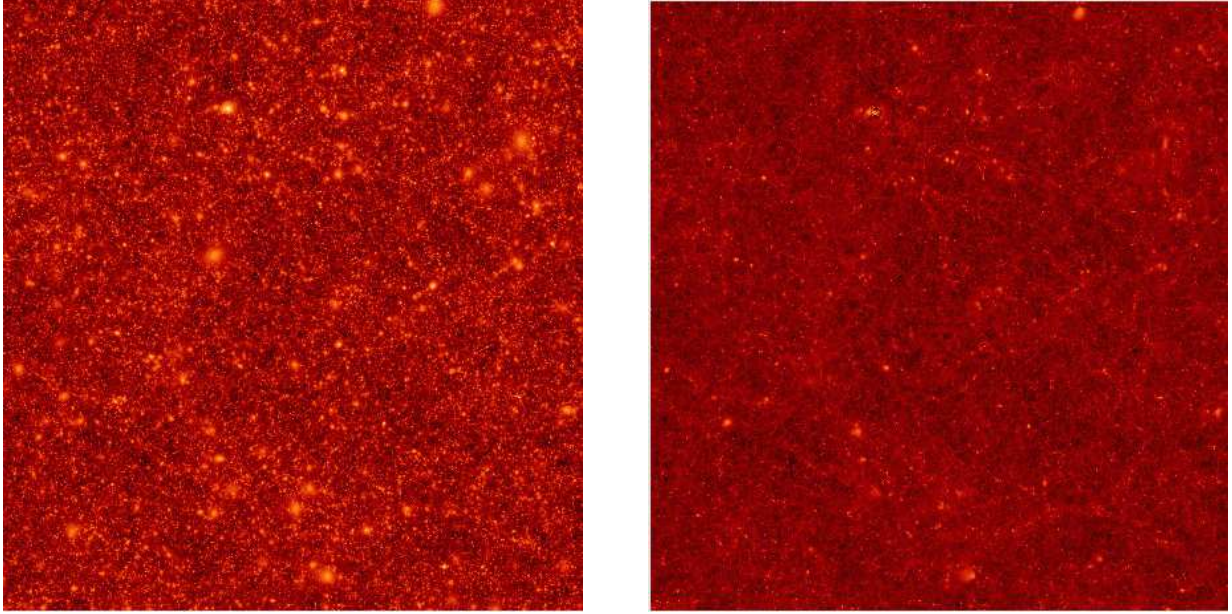


FIG. 10.— Left panel: 100 deg² projected light cone image of the Compton y -parameter from a 512³ *Enzo* simulation of a $(512h^{-1} \text{ Mpc})^3$ volume with 7 dynamic levels of refinement. Light cone includes tiles at 27 discrete redshift intervals between $z=3$ and $z=0.1$. Right panel: Same image as left panel, but with clusters with $M \geq 5 \times 10^{13} M_{\odot}$ cut from the data. Roughly one third of the total flux in the image comes from the objects that remain after the removal of the massive clusters, including poor groups and filaments. We predict that such observations could provide the first detection of the WHIM gas over large sky areas.

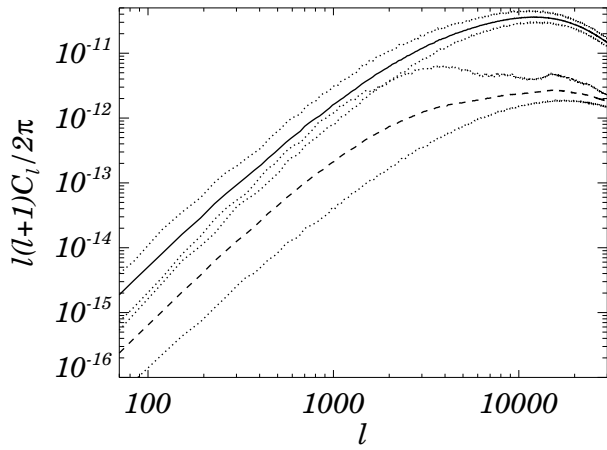


FIG. 11.— Angular power from 200 full light cone images (solid line) compared to angular power from images where $M \geq 5 \times 10^{13} M_{\odot}$ halos are subtracted (dashed line). Dotted lines indicate 90% variance range for the 200 independent stacking realizations of the light cone images.

explored the often neglected contribution of gas in low mass halos and unbound filamentary gas in aggregate to determine the effect on the cluster signal at a single frequency.

The presence of gas outside the cluster virial radii in low density structures such as filaments is potentially an important contributor to the cluster SZE signal. This gas is completely absent in non-hydrodynamic treatments, but appears naturally in our calculation. Since the SZE does not diminish with distance and results from a line of sight integral of the gas pressure, the sum of all the

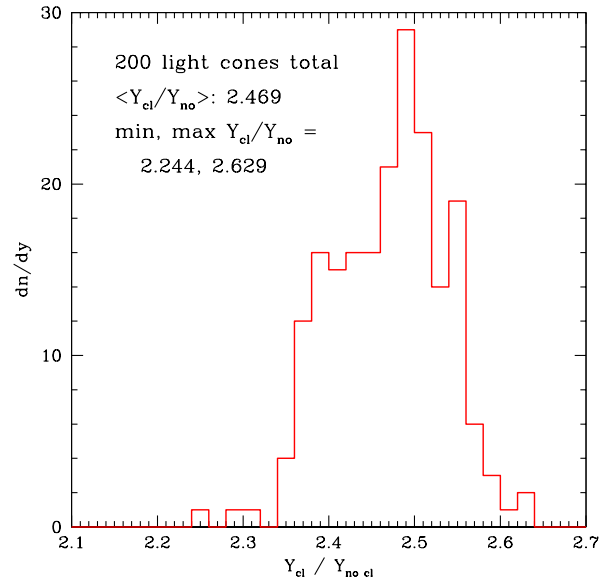


FIG. 12.— Histogram of the ratio of total flux in the SZE y parameter images from clusters with $M \geq 5 \times 10^{13} M_{\odot}$ and from images with clusters subtracted. The histogram is generated from 200 independent realizations of the light cone using the same simulation. Roughly two thirds of the flux in the image comes from clusters with $M \geq 5 \times 10^{13} M_{\odot}$, and the other third comes from the WHIM and poor groups.

flux from unbound gas could be a significant contributor to the total flux in any cluster detection. Additionally, our simulation includes the cluster gas in the full array of dynamically active states. Though the integrated SZE is less sensitive to cluster-cluster merging than an X-ray observation would be, merging contributes non-zero scatter

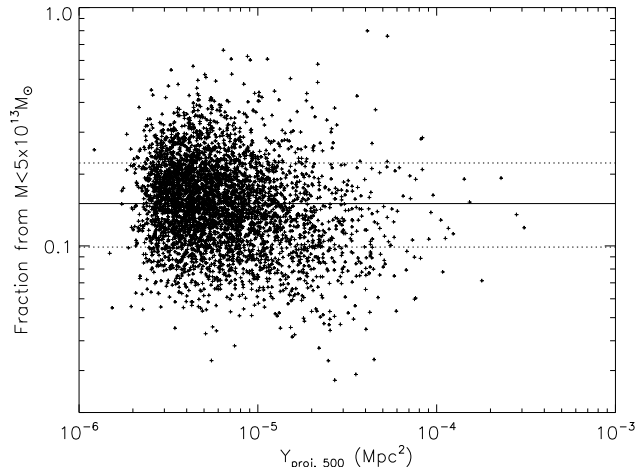


FIG. 13.— Ratio of integrated Compton y inside a cylinder projected to r_{500} from the cluster-subtracted image to integrated Compton y from the same projected cylinder in the full light cone image. Includes all clusters projected into the survey image which have $M \geq 10^{14} M_{\odot}$.

to the Y-M relationship. Thus, for all these reasons it is critically important to self-consistently include baryons in numerical simulations in order to properly simulate sky surveys.

We have shown that on 100 square degree patches of the sky at $l < 2000$ or so the deduced power can be different by factors of 5-8. This indicates that the power spectrum can be quite different from one area of the sky to another, and clearly requires much larger angular areas to be well constrained. The effect of cosmic variance does not become very small until $\ell >$ a few thousand.

We have shown that projection effects can create a large bias and additional scatter in the value of Y measured for clusters of galaxies. For clusters of $M \approx 3.0 \times 10^{14} M_{\odot}$, the median bias in Y due to projection is 79%, and the scatter is +32%/-16% about that median, a significant increase over the scatter in the true Y-M relationship. Additionally, we have shown that the contribution of low-mass unresolved halos and unbound gas to the flux (or decrement) of identified sources can be significant in some cases, and certainly varies widely from source to source. We find that there is a contribution from gas outside clusters of $16.3^{+7.0}_{-6.4}\%$ per object on average for upcoming surveys. This indicates both a bias and an additional source of scatter in the determination of the true SZE signal from any given cluster. As identified by other studies, errors in extracting the correct value of Y should dominate the error budget for the Y-M relation. This effect is critical to understand, since photometric accuracy of the SZE in clusters is key to calibrating a Y-M relationship which can be useful for the precision determination of cosmological parameters. While the intrinsic Y-M relation has very small scatter, what matters in practice is the ability to determine the value of Y accurately. The precision of the calibration of the Y-M relationship depends strongly on its scatter.

We also show results from an analysis of the source confusion for each instrument based on how many massive ($M > 10^{14} M_{\odot}$) clusters lie within an identified source

region (within a radius of r_{500} or a beam diameter at 144 GHz). It appears that pure cluster/group confusion in these surveys will be a significant problem, particularly for Planck Surveyor, but also to a lesser extent for the other single-dish surveys. Smaller beam surveys ($\sim 1'$) have more than one massive cluster within a beam diameter 5-10% of the time, and a larger beam experiment like Planck has multiple clusters per beam 60% of the time. We may have slightly overestimated the problem, since the use of higher resolution (shorter wavelength) bands on some of the survey instruments will help to alleviate this issue. On the other hand, we have not accounted for spurious detections which may result in a field with real backgrounds and instrument noise. Whether this type of confusion can be mitigated depends on a variety of factors, including the mass of the additional secondary objects in the source region, the redshift distribution and angular scale of the objects and the observing beam, and multiple wavelength identification of the objects (e.g., using optical, X-ray, and lensing measurements).

This study uses a large volume, high resolution adiabatic simulation, which serves as a template for more complex runs involving additional non-gravitational physics that is likely important to accurately modeling cluster surveys. There remain important differences between simulation outputs and cluster observations, particularly for lower mass clusters, which indicates the need for a better understanding of the details of baryonic cluster physics. In addition, deviations from isothermality and hydrostatic equilibrium in the cluster gas can have a strong impact on both the observable and derived properties of clusters. It is also important to note that there is some dependence of the SZE signal on the details of the ICM physics (heating, cooling, conduction, etc.) which is not modeled in this work. In future work, we will explore the impact of this additional physics, modeled self-consistently within the hydrodynamic framework of the simulation code, on a selection of SZE clusters from surveys.

This work will be expanded in future papers by a detailed treatment of the point source confusion and instrumental and observing limitations. This will include adding to our synthetic surveys the contribution of the CMB, dusty galaxies, AGN, and atmospheric foreground. We are now working on modeling these, in particular for APEX-SZ and SPT, and will then experiment with matched filtering and the use of multiwavelength coverage provided by SPT for example to mitigate confusion and remove the atmospheric and CMB signals. Matched filtering is a process by which the images are filtered with a kernel matched to the presumed size and shape of the expected sources in the field. In the case of the SZE, this procedure filters out information on larger scales where the primary CMB anisotropies will be a source of confusion. It also maximizes the contrast of the image for the objects at that scale. Since the angular scale subtended by massive clusters is a function of redshift and a weak function of cluster mass, spatial filtering will need to be done at a variety of angular scales to get a complete cluster sample as in Melin et al. (2006). A similar type of analysis has been performed by Sehgal et al. (2006) for ACT's survey.

We also are currently performing additional synthetic light cone sky surveys at X-ray wavelengths, to take a

first look at the limitations of current (e.g. XMM-LSS) and upcoming (e.g. eRosita) X-ray surveys in extracting cosmological parameters.

BWO and MLN have been supported in part by NASA grant NAG5-12140 and NSF grant AST-0307690. BWO has been funded in part under the auspices of the U.S. Dept. of Energy, and supported by its contract W-7405-ENG-36 to Los Alamos National Laboratory. The simulations were by performed at SDSC and NCSA with computing time provided by NRAC allocation MCA98N020. EJH and JOB have been sup-

ported in part by a grant from the U.S. National Science Foundation (AST-0407368). EJH also acknowledges support from NSF AAPF AST-0702923. We thank Yoel Rephaeli for useful discussions on the SZE angular power spectrum. We thank John Carlstrom, Nils Halverson, Jeremiah Ostriker, Douglas Rudd and an anonymous referee for useful comments and critiques. We thank the Aspen Center for Physics for hosting three of the authors during the writing of this manuscript, and also thank Maria's New Mexican Kitchen in Santa Fe for providing an atmosphere conducive to the conception of this project.

REFERENCES

- Berger, M. J. & Colella, P. 1989, *J. Comp. Phys.*, 82, 64
 Bertin, E. & Arnouts, S. 1996, *A&AS*, 117, 393
 Birkinshaw, M. 1999, *Phys. Rep.*, 310, 97
 Bryan, G. & Norman, M. 1997a, 12th Kingston Meeting on Theoretical Astrophysics, proceedings of meeting held in Halifax; Nova Scotia; Canada October 17-19; 1996 (ASP Conference Series # 123), ed. D. Clarke. & M. Fall
 —. 1997b, Workshop on Structured Adaptive Mesh Refinement Grid Methods, ed. N. Chrisochoides (IMA Volumes in Mathematics No. 117)
 Bryan, G. L., Norman, M. L., Stone, J. M., Cen, R., & Ostriker, J. P. 1995, *Comp. Phys. Comm.*, 89, 149
 Carlstrom, J. E., Holder, G. P., & Reese, E. D. 2002, *ARA&A*, 40, 643
 Carroll, S. M., Press, W. H., & Turner, E. L. 1992, *ARA&A*, 30, 499
 Cen, R. & Ostriker, J. P. 2006, *ApJ*, 650, 560
 da Silva, A. C., Barbosa, D., Liddle, A. R., & Thomas, P. A. 2000, *MNRAS*, 317, 37
 Diego, J. M., Vielva, P., Martínez-González, E., Silk, J., & Sanz, J. L. 2002, *MNRAS*, 336, 1351
 Efstathiou, G., Davis, M., White, S. D. M., & Frenk, C. S. 1985, *ApJS*, 57, 241
 Eisenstein, D. J. & Hu, W. 1999, *ApJ*, 511, 5
 Eisenstein, D. J. & Hut, P. 1998, *ApJ*, 498, 137
 Evrard, A. E. 2004, in *Clusters of Galaxies: Probes of Cosmological Structure and Galaxy Evolution, from the Carnegie Observatories Centennial Symposia*. Published by Cambridge University Press, as part of the Carnegie Observatories Astrophysics Series, ed. J. S. Mulchaey, A. Dressler, & A. Oemler, 1–+
 Evrard, A. E., MacFarland, T. J., Couchman, H. M. P., Colberg, J. M., Yoshida, N., White, S. D. M., Jenkins, A., Frenk, C. S., Pearce, F. R., Peacock, J. A., & Thomas, P. A. 2002, *ApJ*, 573, 7
 Fowler, J. W. 2004, in *Z-Spec: a broadband millimeter-wave grating spectrometer: design, construction, and first cryogenic measurements*. Edited by Bradford, C. Matt; Ade, Peter A. R.; Aguirre, James E.; Bock, James J.; Dragovan, Mark; Duband, Lionel; Earle, Lieko; Glenn, Jason; Matsuhara, Hideo; Naylor, Bret J.; Nguyen, Hien T.; Yun, Minhee; Zmuidzinas, Jonas. *Proceedings of the SPIE*, Volume 5498, pp. 1-10 (2004)., ed. C. M. Bradford, P. A. R. Ade, J. E. Aguirre, J. J. Bock, M. Dragovan, L. Duband, L. Earle, J. Glenn, H. Matsuhara, B. J. Naylor, H. T. Nguyen, M. Yun, & J. Zmuidzinas, 1–10
 Geisbüsch, J., Kneissl, R., & Hobson, M. 2005, *MNRAS*, 360, 41
 Güsten, R., Nyman, L. Å., Schilke, P., Menten, K., Cesarsky, C., & Booth, R. 2006, *A&A*, 454, L13
 Haiman, Z., Mohr, J. J., & Holder, G. P. 2001, *ApJ*, 553, 545
 Hallman, E. J. & Markevitch, M. 2004, *ApJ*, 610, L81
 Hallman, E. J., Motl, P. M., Burns, J. O., & Norman, M. L. 2006, *ApJ*, 648, 852
 Heitmann, K., Lukić, Z., Habib, S., & Ricker, P. M. 2006, *ApJ*, 642, L85
 Heitmann, K., Ricker, P. M., Warren, M. S., & Habib, S. 2005, *ApJS*, 160, 28
 Hernández-Montegudo, C., Trac, H., Verde, L., & Jimenez, R. 2006, *ApJ*, 652, L1
 Herranz, D., Sanz, J. L., Barreiro, R. B., & Martínez-González, E. 2002, *ApJ*, 580, 610
 Hobson, M. P. & McLachlan, C. 2003, *MNRAS*, 338, 765
 Hockney, R. W. & Eastwood, J. W. 1988, *Computer Simulation Using Particles* (Institute of Physics Publishing)
 Holder, G., McCarthy, I. G., & Babul, A. 2007, *astro-ph/0702727*
 Holler, C. M. 2000, in *Abstracts from a conference held in Granada, 17-20 of September 2000 and hosted by the Instituto de Radioastronomia Millimetrica (URAM), Universidad de Granada and Instituto de Astrofisica de Andalucia (IAA)*, meeting abstract.
 Itoh, N. & Nozawa, S. 2004, *A&A*, 417, 827
 Jenkins, A., Frenk, C. S., White, S. D. M., Colberg, J. M., Cole, S., Evrard, A. E., Couchman, H. M. P., & Yoshida, N. 2001, *MNRAS*, 321, 372
 Loh, M., Carlstrom, J. E., Cartwright, J. K., Greer, C., Hawkins, D., Hennessy, R., Joy, M., Lamb, J., Leitch, E., Miller, A., Mroczkowski, T., Muchovej, S., Pryke, C., Reddall, B., Richardson, G., Runyan, M., Sharp, M., & Woody, D. 2005, in *Bulletin of the American Astronomical Society*, 1225–+
 Markevitch, M., Gonzalez, A. H., David, L., Vikhlinin, A., Murray, S., Forman, W., Jones, C., & Tucker, W. 2002, *ApJ*, 567, L27
 McCarthy, I. G., Bower, R. G., & Balogh, M. L. 2007, *MNRAS*, 377, 1457
 Melin, J.-B., Bartlett, J. G., & Delabrouille, J. 2006, *A&A*, 459, 341
 Motl, P. M., Burns, J. O., Loken, C., Norman, M. L., & Bryan, G. L. 2004, in *Clusters of Galaxies: Probes of Cosmological Structure and Galaxy Evolution*, ed. J. S. Mulchaey, A. Dressler, & A. Oemler
 Motl, P. M., Hallman, E. J., Burns, J. O., & Norman, M. L. 2005, *ApJ*, 623, L63
 Murdin, P. 2000, *Encyclopedia of Astronomy and Astrophysics*
 Nagai, D. 2006, *ApJ*, 650, 538
 Norman, M. & Bryan, G. 1999, *Numerical Astrophysics : Proceedings of the International Conference on Numerical Astrophysics 1998 (NAP98)*, held at the National Olympic Memorial Youth Center, Tokyo, Japan, March 10-13, 1998., ed. K. T. S. M. Miyama & T. Hanawa (Kluwer Academic)
 O'Shea, B., Bryan, G., Bordner, J., Norman, M., Abel, T., & Harkness, R. and Kritsuk, A. 2004, *Adaptive Mesh Refinement - Theory and Applications*, ed. T. Plewa, T. Linde, & G. Weirs (Springer-Verlag)
 O'Shea, B. W., Nagamine, K., Springel, V., Hernquist, L., & Norman, M. L. 2005, *ApJS*, 160, 1
 Peebles, P. J. E. 1993, *Principles of physical cosmology* (Princeton Series in Physics, Princeton, NJ: Princeton University Press, —c1993)
 Press, W. H. & Schechter, P. 1974, *ApJ*, 187, 425
 Randall, S. W., Sarazin, C. L., & Ricker, P. M. 2002, *ApJ*, 577, 579
 Rasia, E., Ettori, S., Moscardini, L., Mazzotta, P., Borgani, S., Dolag, K., Tormen, G., Cheng, L. M., & Diaferio, A. 2006, *MNRAS*, 369, 2013
 Rasia, E., Mazzotta, P., Borgani, S., Moscardini, L., Dolag, K., Tormen, G., Diaferio, A., & Murante, G. 2005, *ApJ*, 618, L1
 Reed, D., Governato, F., Quinn, T., Gardner, J., Stadel, J., & Lake, G. 2005, *MNRAS*, 359, 1537

- Rephaeli, Y. 1995, *ARA&A*, 33, 541
- Ricker, P. M. & Sarazin, C. L. 2001, *ApJ*, 561, 621
- Roettiger, K., Burns, J. O., & Loken, C. 1996, *ApJ*, 473, 651
- Roncarelli, M., Moscardini, L., Borgani, S., & Dolag, K. 2007, *ArXiv Astrophysics e-prints*, astro-ph/0701680
- Roncarelli, M., Moscardini, L., Tozzi, P., Borgani, S., Cheng, L. M., Diaferio, A., Dolag, K., & Murante, G. 2006, *MNRAS*, 368, 74
- Rosati, P., Borgani, S., & Norman, C. 2002, *ARA&A*, 40, 539
- Ruhl, J., Ade, P. A. R., Carlstrom, J. E., Cho, H.-M., Crawford, T., Dobbs, M., Greer, C. H., Halverson, N. w., Holzappel, W. L., Lanting, T. M., Lee, A. T., Leitch, E. M., Leong, J., Lu, W., Lueker, M., Mehl, J., Meyer, S. S., Mohr, J. J., Padin, S., Plagge, T., Pryke, C., Runyan, M. C., Schwan, D., Sharp, M. K., Spieler, H., Staniszewski, Z., & Stark, A. A. 2004, in *Z-Spec: a broadband millimeter-wave grating spectrometer: design, construction, and first cryogenic measurements*. Edited by Bradford, C. Matt; Ade, Peter A. R.; Aguirre, James E.; Bock, James J.; Dragovan, Mark; Duband, Lionel; Earle, Lieko; Glenn, Jason; Matsuhara, Hideo; Naylor, Bret J.; Nguyen, Hien T.; Yun, Minhee; Zmuidzinas, Jonas. *Proceedings of the SPIE*, Volume 5498, pp. 11-29 (2004)., ed. C. M. Bradford, P. A. R. Ade, J. E. Aguirre, J. J. Bock, M. Dragovan, L. Duband, L. Earle, J. Glenn, H. Matsuhara, B. J. Naylor, H. T. Nguyen, M. Yun, & J. Zmuidzinas, 11–29
- Schäfer, B. M., Pfrommer, C., Hell, R. M., & Bartelmann, M. 2006, *MNRAS*, 370, 1713
- Schulz, A. E. & White, M. 2003, *ApJ*, 586, 723
- Sehgal, N., Trac, H., Huffenberger, K., & Bode, P. 2006, *ArXiv Astrophysics e-prints*
- Sheth, R. K. & Tormen, G. 1999, *MNRAS*, 308, 119
- Springel, V., Frenk, C. S., & White, S. D. M. 2006, *Nature*, 440, 1137
- Springel, V., White, M., & Hernquist, L. 2001, *ApJ*, 549, 681
- Stone, J. M. & Norman, M. L. 1992a, *ApJS*, 80, 753
- . 1992b, *ApJS*, 80, 791
- Sunyaev, R. A. & Zeldovich, Y. B. 1972, *Comments on Astrophysics and Space Physics*, 4, 173
- Tozzi, P. 2006, *ArXiv Astrophysics e-prints*, astro-ph/0602072
- Vikhlinin, A., Markevitch, M., Murray, S. S., Jones, C., Forman, W., & Van Speybroeck, L. 2005, *ApJ*, 628, 655
- Wang, L. & Steinhardt, P. J. 1998, *ApJ*, 508, 483
- Warren, M. S., Abazajian, K., Holz, D. E., & Teodoro, L. 2006, *ApJ*, 646, 881
- White, M., Hernquist, L., & Springel, V. 2002, *ApJ*, 579, 16
- White, S. 2003, *The Cosmic Cauldron*, 25th meeting of the IAU, Joint Discussion 10, 18 July 2003, Sydney, Australia, 10
- Woodward, P. R. & Colella, P. 1984, *J. Comp. Phys.*, 54, 174